RSC Advances

PAPER

View Article Online
View Journal | View Issue

Check for updates

Cite this: *RSC Adv.*, 2022, **12**, 16823

# Near-perfect spectrally-selective metasurface solar absorber based on tungsten octagonal prism array†

Mingpan Xu,[a] Lin Guo,[b] Pengfei Zhang,[a] Yu Qiu,*[a] Qing Li*[a] and Jikang Wang[a]

Solar selective absorbers influence the photothermal efficiency of high-temperature solar thermal applications directly and significantly. In present work, a metasurface absorber consisting of an octagonal prism array is proposed, optimized and analyzed. Firstly, the structure parameters of the absorber are optimized, finding the optimal absorber achieves near-perfect spectrally-selectivity compared with the perfect solar absorber. The high solar absorptivity of 0.9591, low emissivity of 0.1594–0.3694, and high photothermal efficiency of 94.72–83.10% are achieved at 1073–1573 K and 1000 suns. Then, the mechanisms leading to the excellent spectral selectivity are investigated, suggesting that the coupling effects of multi-plasmon resonance modes and the impedance matching lead to the high solar absorptivity. Meanwhile, the impedance mismatching is the mechanism to minimize the emissivity in the mid-IR region. Moreover, whether the spectral absorptivity can be changed by structural parameters is investigated, suggesting that the excircle diameter of the first tungsten octagonal prism and the height of $SiO_2$ under the octagonal prism can influence the spectral absorptivity obviously. Finally, the metasurface absorber is demonstrated to be highly insensitive to both polarization and incident angles. These results suggest that the proposed metasurface absorber should be suitable for high-temperature solar thermal devices.

Received 3rd May 2022
Accepted 30th May 2022

DOI: 10.1039/d2ra02802f

rsc.li/rsc-advances

Open Access Article. Published on 07 June 2022. Downloaded on 7/28/2024 11:16:37 PM.
This article is licensed under a Creative Commons Attribution-NonCommercial 3.0 Unported Licence.

## 1. Introduction

Solar energy, as an abundant, clean, and sustainable renewable energy, has gained much attention in recent years because of its ability to alleviate energy shortage and reduce environmental pollution from fossil fuels.[1–3] Concentrated solar power is a promising technology that generates electricity through solar-thermal conversion and thermal-driven power cycle.[4] To improve the power cycle efficiency, the temperature of the solar–thermal conversion has been increased continuously during the last two decades.[55] Recently, a solar power tower system with graphite-based receiver has even been proposed to operate at above 1300 °C.[5,54] However, the radiative thermal loss from the solar absorber increases with the fourth power of temperature, reducing the photothermal efficiency of the absorber significantly.[56,57] To ensure that the solar-electric efficiency, which is the product of the photothermal efficiency and the power cycle efficiency, can be improved effectively under high temperature, the photothermal efficiency is necessary to be as high as possible.

To enhance the photothermal efficiency, the absorber should exhibit high absorptivity in the solar spectrum and low emissivity in the mid-IR region (*i.e.* good spectral selectivity).[6] However, there are two problems with present state-of-the-art commercial Pyromark absorber when the temperature rises to 1300 °C. Firstly, the solar absorptivity of this commercial absorber is as high as 0.965 within the solar spectrum, but its spectral emissivity also can be as high as ~0.85 within the mid-IR region.[53] Meanwhile, this absorber cannot withstand the high temperature of above 1100 °C.

To solve the two problems, many absorbers have been proposed in the literature, which can be roughly divided into multilayered absorbers and metasurface absorbers (MAs).

The multilayered absorbers were usually designed to utilize the interference effects among different layers to achieve good spectral selectivity.[7] For example, He *et al.* designed a $SiO_2$/AlCrTaTiZrN absorber, obtaining the high solar absorptance ($\alpha_{sol}$) of 0.928 and high photothermal efficiency ($\eta$) of 87.7% at 873 K, when the solar concentration ratio is 100.[8] Qiu *et al.* fabricated a $HfB_2/TiB_2$ absorber, which could achieve a high $\alpha_{sol}$ of 0.932 and a high $\eta$ of 68.6% at 1073 K, when the solar concentration ratio is 100.[9] Atasi *et al.* reported a W/WAlN/WAlON/$Al_2O_3$ absorber with the $\alpha_{sol}$ of 0.90, and its $\varepsilon_{tot}$ is as low as 0.15 at 773 K.[10] Nuru *et al.* fabricated an Al*x*Oy/Pt/Al*x*Oy multilayer absorber, obtaining the $\alpha_{sol}$ of 0.951, and the $\varepsilon_{tot}$ is as low as 0.08 at 773 K.[11] Tian *et al.* investigated a multilayered

[a]*School of Energy Science and Engineering, Central South University, Changsha, Hunan, 410083, China. E-mail: yu.qiu@csu.edu.cn; qingli@csu.edu.cn*

[b]*Energy Research Institute, Qilu University of Technology, Jinan, 250014, P. R. China*

† Electronic supplementary information (ESI) available. See https://doi.org/10.1039/d2ra02802f

© 2022 The Author(s). Published by the Royal Society of Chemistry

Open Access Article. Published on 07 June 2022. Downloaded on 7/28/2024 11:16:37 PM.
This article is licensed under a Creative Commons Attribution-NonCommercial 3.0 Unported Licence.

stack consisting of $SiO_2/Al_2O_3/W/Al_2O_3/W$, founding that the $\alpha_{sol}$ and the photothermal efficiency ($\eta$) of it are 0.881 and 82.3% at 673 K, respectively, when the solar concentration ratio is 100.[12] Wang *et al.* demonstrated a $SiO_2$–$Si_3N_4$ multilayer, which could obtain the spectral absorptivity ($\alpha_\lambda$) of 0.95 in the solar spectrum and the spectral emissivity of 0.1 in the mid-IR region.[13] AL-Rjoub *et al.* deposited a $WSiAlN_x/WSiAlO_yN_x$ multilayer absorber with the $\alpha_{sol}$ as high as 0.96 and the $\varepsilon_{tot}$ as low as 0.11 at 673 K.[14] Wang *et al.* developed a Cr/AlCrN/AlCrNO/AlCrO multilayer absorber, and the results showed that the $\alpha_{sol}$ of 0.94 and the $\varepsilon_{tot}$ of 0.25 at 773 K are obtained.[15]

The metasurface absorbers (MAs) were designed to obtain good spectral selectivity through exciting different resonance modes. The geometries of these MAs were designed to possess the sizes equivalent to incident wavelengths to obtain good spectral selectivity through the excitation of multi-plasmon resonance modes. For example, Zhao *et al.* designed a MA based on C–Si trapezoidal pyramids and Al pyramids, and the results indicated that the average $\alpha_\lambda$ of 0.9316 within 0.3–1.4 μm was obtained owing to the excitation of Surface Plasmon Polaritons (SPPs).[16] Zhou *et al.* proposed a MA consisting of $SiO_2/Si_3N_4$/Ti substrate and Ti rings, which could achieve the average $\alpha_\lambda$ of 0.9 within 0.3–4 μm and the $\alpha_{sol}$ of 0.97 by enhancing the synergistic effects of the plasmon resonances.[17] Liu *et al.* reported a MA based on a TiN disk array, achieving the $\alpha_\lambda$ higher than 0.90 within 0.316–1.426 μm due to the excitation of plasmonic resonances and their hybrid coupling effects.[18] Chen *et al.* investigated a MA consisting of Ni disks, obtaining the $\alpha_{sol}$ of above 0.90 and the $\eta$ of as high as 89.01% at 800 K by coupling the SPPs, Magnetic Polaritons (MPs), and the intrinsic absorption of Ni.[19] Wu *et al.* proposed a MA based on nanoporous W/$SiO_2$ film, and the results indicated that the $\eta$ of 90.32% at 800 K is obtained owing to the impedance matching with the free space.[20] Jiang *et al.* designed a MA by combining a planar multilayer system and a nanowire array, obtaining the average $\alpha_\lambda$ of above 0.9 within the wavelength of 0.3–1.909 μm due to the coupling effects of multiple resonance modes.[21] Hassan *et al.* designed a MA based on nanowire array, which could achieve the average $\alpha_\lambda$ of 0.97 at the wavelength of 0.3–1.3 μm.[22]

To sum up, even though many solar selective absorbers have been proposed and investigated, however, there are still many problems with these absorbers. Firstly, the photothermal conversion performance of the absorbers has not reached the ideal value. Then, the thermal stability of the absorbers under high temperatures remains relatively low. Finally, the complex structures of some absorbers are difficult to manufacture. Therefore, designing a simple solar absorber that can be easily manufactured and can obtain excellent photothermal conversion performance, eminent thermal stability, incident and polarization angle insensitivity is still a challenging task.

In this article, a spectrally-selective metasurface absorber (MA) based on tungsten octagonal prisms was proposed and investigated. Firstly, structure parameters of the proposed MA were optimized to achieve good spectral selectivity and high photothermal efficiency. Next, a three-dimensional simulation of the electromagnetic fields revealed the physical absorption mechanisms of the MA. In addition, the influences of the structure parameters on the absorption performance were investigated. Finally, the influences of changes in polarization and incident angles were explored. The novelty of this work is that an absorber with simple structure was proposed, and it was proved to be able to achieve higher photothermal efficiency than ten new absorbers proposed within the last five years at various operating conditions. It is well known that 1% improved photothermal efficiency can improve the output of the plant by 0.9–1.4% while keeping investment constant.[23] Thus, the proposed absorber is promising to improve the performance of the plant.

## 2. Design of the metasurface absorber

The metasurface absorber (MA) proposed for high-temperature solar applications is composed of many structural units which are arranged in a periodic way (see Fig. 1a and b). As illustrated in Fig. 1c, the components of the structural unit (see Fig. 1c) are the first and the second tungsten films, the first and the second $SiO_2$ films, the first and the second tungsten octagonal prisms, and the $SiO_2$ octagonal prism. Moreover, considerations for designing different components of the MA are detailed as follows.

Firstly, the first $SiO_2$ film between the first and the second tungsten films was designed to produce magnetic polaritons.[24] Then, the tungsten octagonal prism array, the second $SiO_2$ film,

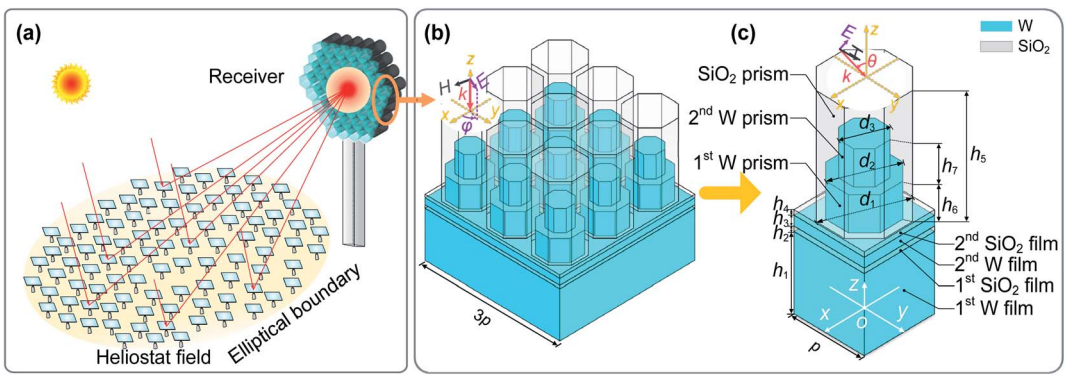


Fig. 1 (a) Sketch of a concentrated solar collector; (b) 3D structure of the designed MA; (c) a structural unit.


© 2022 The Author(s). Published by the Royal Society of Chemistry

Open Access Article. Published on 07 June 2022. Downloaded on 7/28/2024 11:16:37 PM.
This article is licensed under a Creative Commons Attribution-NonCommercial 3.0 Unported Licence.

and the second tungsten film were constructed to excite magnetic polaritons as well. Then, localized surface plasmon resonances (LSPRs) will be excited at the vertex of the tungsten octagonal prism.[25] Furthermore, at the upper surface of the first and the second tungsten octagonal prisms, surface plasmon polaritons were excited.[25] In addition, the $SiO_2$ octagonal prisms that wrap the tungsten octagonal prisms were constructed to prevent the tungsten from being oxidized and grain growth.[26] Moreover, the melting points of the tungsten and $SiO_2$ are 3673 K and 1996 K, respectively, which are much higher than 1573 K. Hence, the proposed absorber will possess excellent thermal stability. Finally, the designed structure can be fabricated by some mature techniques such as ICP etching, magnetic sputterings, atomic layer deposition, and electron-beam lithography.[27]

Besides, the structure parameters of the proposed MA are also shown in Fig. 1. Where $h_1$, $h_2$, $h_3$, $h_4$, $h_5$, $h_6$, and $h_7$ are the heights of different components, and $d_1$, $d_2$, and $d_3$ are the excircle diameters of the $SiO_2$ octagonal prism, the first and the second tungsten octagonal prisms, respectively. $p$ is the periodicity of the structural unit. In the following sections, firstly, the finite element method is used to calculate the spectral absorptivity of the MA under different structure parameters. Then, the structure parameters would be optimized based on orthogonal experiments to make the spectral selectivity reach the best at high temperature.

## 3. Simulation methods

A finite element model was developed by solving Maxwell's equations that can describe the solar radiation transport in the proposed MA.[28] Owing to the symmetric structure of the MA, only a unit (seen in Fig. 1c) is simulated in the model. In the model, the effects of wavelength on the refractive indexes of the tungsten and $SiO_2$ are considered,[29,30] as shown in Fig. S1 in the ESI.†[24,25] The transport process of the light in the MA can be described by the Maxwell's equations, which was solved by finite element method using a commercially available software package COMSOL Multiphysics 5.6.[31]

The boundary conditions on the boundaries perpendicular to the $x$-axis and $y$-axis are Floquet periodicity boundary conditions. In addition, the boundary conditions on the top surface and bottom surface are port conditions. The port condition on the top surface is used to emit solar radiation into the MA, and the incident angle ($\theta$) and polarization angle ($\varphi$) are shown in Fig. 1b and c. The port condition on the bottom surface is used to calculate the transmitted radiation. The height of the first tungsten film ($h_1$) is set to be 150 nm, which exceeds the penetration depth of incident radiation. Therefore, solar radiation cannot penetrate the MA, which has the spectral transmittance ($\tau_\lambda$) of zero. The spectral absorptivity ($\alpha_\lambda$) and spectral reflectance ($\rho_\lambda$) of the MA can be calculated by eqn (1) and (2).[32,33]

$$\rho_\lambda = |S_{11}|^2 \tag{1}$$

$$\alpha_\lambda = 1 - \rho_\lambda \tag{2}$$

where $S_{11}$ is the scattering matrix coefficient of the reflection.

Some parameters are defined for evaluating the performance of the MA. The solar absorptivity ($\alpha_{sol}$) equals the proportion of the absorbed solar radiation in the incident solar radiation, as shown in eqn (3).[34] The total emissivity ($\varepsilon_{tot}$) equals to the ratio of the radiative power values radiated by the MA and blackbody, as illustrated in eqn (4).[23] The photothermal efficiency ($\eta$) equals the ratio of solar radiation transformed into thermal energy and the incident solar radiation, as shown in eqn (5).[35]

$$\alpha_{sol} = \frac{\int_{0.28\ \mu m}^{4\ \mu m} \alpha_\lambda I_{AM1.5}(\lambda) d\lambda}{\int_{0.28\ \mu m}^{4\ \mu m} I_{AM1.5}(\lambda) d\lambda} \tag{3}$$

$$\varepsilon_{tot} = \frac{\int_{0.28\ \mu m}^{50\ \mu m} \alpha_\lambda I_B(\lambda, T_{abs}) d\lambda}{\int_{0.28\ \mu m}^{50\ \mu m} I_B(\lambda, T_{abs}) d\lambda} \tag{4}$$

$$\eta = \alpha_{sol} - \frac{5.67 \times \varepsilon_{tot}\left(T_{abs}^4 - T_{amb}^4\right)}{CI_s \times 10^8} \tag{5}$$

where $T_{abs}$, $T_{amb}$, $C$ and $I_s$ are the temperature of MA, temperature of ambient, solar concentration ratio and solar flux intensity at AM1.5, respectively; $I_{AM1.5}(\lambda)$ is the spectral solar irradiance at AM1.5;[36] $I_B(\lambda, T_{abs})$ is the spectral irradiance of blackbody at $T_{abs}$, which is calculated by Planck's radiation law, as shown in eqn (6).[37]

$$I_B(\lambda, T_{abs}) = \frac{3.7419 \times 10^{-16}}{\lambda^5\left(e^{1.4388 \times 10^{-2}/(\lambda T)} - 1\right)} \tag{6}$$

To make sure that the simulation results are insensitive to the mesh number, grid independence tests have been performed as illustrated in Table S1 in the ESI.† To validate the current model, the model have been verified through comparing the results calculated by the present model and Han *et al.*'s model, as shown in Fig. S2 in the ESI.† The results indicate that the present model can be considered reliable.

## 4. Results and discussion

In the following paragraphs, firstly, a near-perfect metasurface absorber (MA) is designed by optimizing its structure parameters. Next, the underlying absorption mechanisms giving rise to the near-perfect spectrally-selectivity of the MA were revealed and analyzed. Then, the influences of structure parameters on the performance were illustrated. Finally, sensitivities of the MA to incident angle and polarization angle were studied. In addition, it is worth noting that the incident light defaults to be normally incident TM polarized wave.

### 4.1 Near-perfect spectrally-selective metasurface absorber

The structures of the metasurface absorber (MA) were optimized by orthogonal tests to obtain good spectral selectivity and solar-thermal conversion performance. In the optimization, the photothermal efficiency ($\eta$) under 1573 K and 1000 suns was selected as the object function. After the optimization, a optimal MA with the structure parameters of $p = 155$ nm, $h_1 =$

Open Access Article. Published on 07 June 2022. Downloaded on 7/28/2024 11:16:37 PM.
This article is licensed under a Creative Commons Attribution-NonCommercial 3.0 Unported Licence.

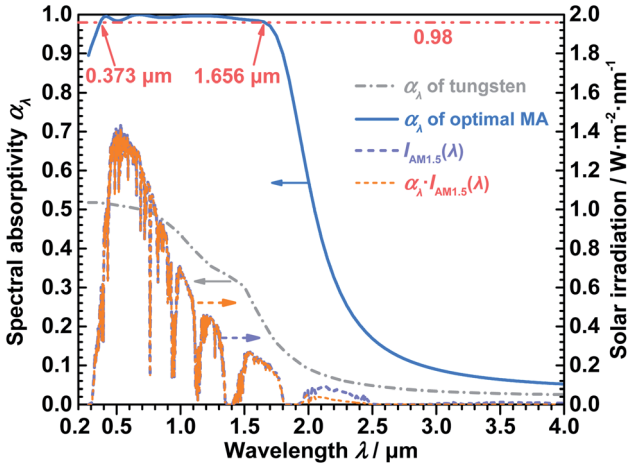


Fig. 2 AM1.5 solar spectrum and spectral absorptivity of the optimal MA.

150 nm, $h_2 = 10$ nm, $h_3 = 20$ nm, $h_4 = 10$ nm, $d_1 = 150$ nm, $h_5 = 240$ nm, $d_2 = 130$ nm, $h_6 = 70$ nm, $d_3 = 80$ nm and $h_7 = 70$ nm was obtained.

The AM1.5 solar spectrum and spectral absorptivity of the optimal MA are demonstrated in Fig. 2. It can be found that the $\alpha_\lambda$ is above 0.9 at the wavelength of 0.285–1.8 μm. Specifically, the $\alpha_\lambda$ even exceeds 0.98 at the wavelength of 0.373–1.656 μm. According to eqn (3), the optimal MA achieves an excellent solar absorptivity ($\alpha_{sol}$) of 0.9591. In addition, the $\alpha_\lambda$ of a 150 nm tungsten film was also simulated and compared with the optimal MA. As shown in Fig. 2, the $\alpha_\lambda$ of tungsten is 0.3773–0.7885 lower than that of the optimal MA within 0.285–1.8 μm. Meanwhile, the $\alpha_{sol}$ of tungsten is 0.5189 lower than that of the optimal MA, indicating that the reasonable design of the optimal MA has improved the optical performance of tungsten greatly. It also can be found in Fig. 2 that the $\alpha_\lambda$ drops sharply with increasing $\lambda$ when $\lambda > 1.8$ μm, and therefore the $\alpha_\lambda$ even becomes below 0.06 when $\lambda > 3.616$ μm. To sum up, the optimal MA exhibits high absorptivity in the solar spectrum and low emissivity in the mid-IR region.

In addition, the total emissivity ($\varepsilon_{tot}$) and photothermal efficiency ($\eta$) under different MA temperatures ($T_{abs}$) when $T_{amb} = 300$ K and $C = 1000$ suns were calculated through eqn (4) and (5) to further demonstrate the spectral selectivity of the optimal MA. It can be observed from Table 1 that the $\varepsilon_{tot}$ increases with increasing $T_{abs}$, and $\varepsilon_{tot}$ is within 0.1594–0.3694 when $T_{abs} =$ 1073–1573 K. Besides, $\eta$ decreases with increasing $T_{abs}$, and $\eta$ is within 83.10–94.72% when $T_{abs} =$ 1073–1573 K.

Table 1 Performance of the optimal MA under different temperatures

| | | | Current optimal MA | | Perfect absorber | |
|---|---|---|---|---|---|---|
| $C$/suns | $T_{abs}$/K | $T_{amb}$/K | $\varepsilon_{tot}$ | $\eta$ | $\varepsilon_{tot}$ | $\eta$ |
| 1000 | 1073 | 300 | 0.1594 | 94.72% | 0.3487 | 96.39% |
| 1000 | 1173 | 300 | 0.1990 | 93.78% | 0.3753 | 94.72% |
| 1000 | 1273 | 300 | 0.2410 | 92.32% | 0.1813 | 92.85% |
| 1000 | 1373 | 300 | 0.2841 | 90.20% | 0.2214 | 91.07% |
| 1000 | 1473 | 300 | 0.3272 | 87.19% | 0.2564 | 88.54% |
| 1000 | 1573 | 300 | 0.3694 | 83.10% | 0.2907 | 85.08% |

For a perfect solar absorber, it should achieve the highest $\eta$ under the corresponding working conditions.[38] When the wavelength is smaller than a truncation wavelength, its $\alpha_\lambda$ should be 1. When the wavelength is larger than the truncation wavelength, the its $\alpha_\lambda$ should be 0.[39] The $\varepsilon_{tot}$ and $\eta$ of the perfect absorber under different $T_{abs}$ are also calculated when $T_{amb} =$ 300 K and $C = 1000$ suns, and the results are shown in Table 1. As illustrated in Table 1, the $\varepsilon_{tot}$ of the optimal MA is just 0.0597–0.0787 larger than that of the perfect absorber when $T_{abs}$ = 1273–1573 K. Moreover, the $\eta$ of the optimal MA is just 0.53–0.1.98% lower than that of the perfect absorber when $T_{abs} =$ 1073–1573 K. Thus, it is concluded that the optimal MA can convert solar energy to thermal energy efficiently at high temperatures, and the spectral selectivity is almost the same as that of the perfect absorber. Hence, the optimal MA can be considered as a near-perfect spectrally-selective absorber.

Furthermore, the performance of the near-perfect MA was compared with that of some previously developed absorbers in Table 2. As can be seen in Table 2, Wu *et al.* designed a MA based on nanoporous W/$SiO_2$ film, which can obtain the $\eta$ of 90.32% that is 2.52% lower than the 92.84% of the near-perfect MA when $C = 1$ and $T_{abs} = 373$ K.[20] Wang *et al.* reported an absorber using manganese-iron oxide nanoparticles, achieving the $\eta$ of 89.30% that is 5.74% lower than the 95.04% of the present near-perfect MA under $C = 1000$ and $T_{abs} = 1023$ K.[40] Niranjan *et al.* studied a W/WAlSiN/SiON/$SiO_2$ multilayer, which can obtain the $\eta$ of 89.50% that is 5.01% lower than the 94.51% of the near-perfect MA when $C = 100$ and $T_{abs} = 773$ K.[41] He *et al.* studied an absorber based on alloy nitride MoTaTiCrN nanofilms, obtaining the $\eta$ of 86.90% that is 6.92% lower than the 93.82% of the near-perfect MA under $C = 100$ and $T_{abs} = 823$ K.[42] Ye *et al.* reported an absorber based on a tungsten sphere and cuboid array, which can achieve the $\eta$ of 87.56% that is 0.81% lower than the 88.37% of the near-perfect MA when $C =$ 100 and $T_{abs} = 1000$ K.[43] Zhang *et al.* designed a chimney-like absorber, which can obtain the $\eta$ of 91.62% that is 1.83% lower than the 93.45% of the near-perfect MA when $C = 1000$ and $T_{abs} = 1200$ K.[44] Li *et al.* reported an absorber based on TiN particles, obtaining the $\eta$ of 93.00% that is 1.12% lower than the 94.12% of the near-perfect MA when $C = 1$ and $T_{abs} = 373$ K.[45] Zhao *et al.* proposed a $Al_{0.4}Hf_{0.6}$NbTaTiZrN MA, which can achieve the $\eta$ of 74.90% that is 20.45% lower than the 95.35% of the near-perfect MA under $C = 100$ and $T_{abs} = 673$ K.[46] Raza *et al.* designed an absorber using SiC–W nanoparticles, achieving the $\eta$ of 82.68% that is 3.13% lower than the 85.81% of the near-perfect MA under $C = 100$ and $T_{abs} = 1050$ K.[47] Qiu *et al.* studied an absorber based on $TiB_2$–$ZrB_2$ composite ceramic, which can obtain the $\eta$ of 83.90% that is 10.61% lower than the 94.51% of the near-perfect MA when $C = 100$ and $T_{abs} =$ 773 K.[48] He *et al.* reported a double-layer alloy nitride HfNbTaTiZrN absorber, obtaining the $\eta$ of 90.10% that is 3.75% lower than the 93.85% of the near-perfect MA under $C = 100$ and $T_{abs} = 823$ K.[49] The above mentioned results demonstrate


© 2022 The Author(s). Published by the Royal Society of Chemistry

Open Access Article. Published on 07 June 2022. Downloaded on 7/28/2024 11:16:37 PM. This article is licensed under a Creative Commons Attribution-NonCommercial 3.0 Unported Licence.

Table 2 Performance comparisons of the near-perfect MA and some existing absorbers

| Absorber | $C$ | $T_{abs}$/K | $T_{amb}$/K | $\alpha_{sol}$ | $\varepsilon_{tot}$ | $\eta$ |
|---|---|---|---|---|---|---|
| Present | 1 | 373 K | 0 | 0.9591 | 0.2800 | 92.84% |
| Ref. 20 | 1 | 373 K | 0 | — | — | 90.32% |
| Present | 1000 | 1023 | 300 | 0.9591 | 0.1410 | 95.04% |
| Ref. 40 | 1000 | 1023 | 300 | 0.9270 | 0.5500 | 89.30% |
| Present | 100 | 773 | 0 | 0.9591 | 0.0693 | 94.51% |
| Ref. 41 | 100 | 773 | 0 | 0.9550 | 0.1570 | 89.50% |
| Present | 100 | 823 | 300 | 0.9591 | 0.0805 | 93.82% |
| Ref. 42 | 100 | 823 | 300 | 0.9230 | 0.0650 | 86.90% |
| Present | 100 | 1000 | 0 | 0.9591 | 0.1329 | 88.37% |
| Ref. 43 | 100 | 1000 | 0 | 0.9535 | 0.1375 | 87.56% |
| Present | 1000 | 1273 | 300 | 0.9591 | 0.2102 | 93.45% |
| Ref. 44 | 1000 | 1273 | 300 | 0.9457 | 0.2056 | 91.62% |
| Present | 1 | 373 | 300 | 0.9591 | 0.0280 | 94.12% |
| Ref. 45 | 1 | 373 | 300 | 0.9500 | 0.0300 | 93.00% |
| Present | 100 | 673 | 300 | 0.9591 | 0.0503 | 95.35% |
| Ref. 46 | 100 | 673 | 300 | 0.8600 | 0.1950 | 74.90% |
| Present | 100 | 1050 | 300 | 0.9591 | 0.1475 | 85.81% |
| Ref. 47 | 100 | 1050 | 300 | 0.9545 | 0.2000 | 82.68% |
| Present | 100 | 773 | 0 | 0.9591 | 0.0693 | 94.51% |
| Ref. 48 | 100 | 773 | 0 | 0.9340 | 0.2320 | 83.90% |
| Present | 100 | 823 | 300 | 0.9591 | 0.0805 | 93.85% |
| Ref. 49 | 100 | 823 | 300 | 0.9600 | 0.2250 | 90.10% |

that the photothermal conversion performance of the present near-perfect MA is better than some previously absorbers.

### 4.2 Mechanisms for the spectrally-selective characteristics

To reveal the mechanisms of the excellent spectral selectivity and the good photothermal performance of the near-perfect MA, the transmission and absorption of solar radiation in the near-perfect MA is simulated. The distributions of the magnitudes of electromagnetic fields and Poynting vectors, the impedance matching between the MA and the free space, and the spectral absorptivity of different components were studied, and the results are as follows.

Firstly, to reveal the dissipation mechanisms of electromagnetic waves within the MA, the Poynting vectors and the distributions of the magnitudes of the electric field ($|\boldsymbol{E}|$) and magnetic field ($|\boldsymbol{H}|$) were illustrated in Fig. 3.

Fig. 3a and b describe the $|\boldsymbol{E}|$ and $|\boldsymbol{H}|$ distributions in the $xz$ plane at $y = 0$, respectively. As shown in Fig. 3a and b, there are four regions with strong $|\boldsymbol{E}|$ at both sides of the first and second tungsten octagonal prisms, and three regions with strong $|\boldsymbol{H}|$ appear at the upper surface of the first and second tungsten octagonal prisms. These results suggest the excitation of surface plasmon polaritons (SPPs) at the top of the first and the second tungsten octagonal prisms. In addition, two regions with strong $|\boldsymbol{E}|$ arise at the edges of the bottom of the second tungsten octagonal prism, and two regions with strong $|\boldsymbol{H}|$ arise at the first and second $SiO_2$ films. The $|\boldsymbol{E}|$ and $|\boldsymbol{H}|$ at these regions increase with rising wavelength. These results implicate that magnetic polaritons (MPs) are excited at the first and second $SiO_2$ films, and the intensity of MPs increases with rising wavelength.

Then, because the $xy$ planes at $z = 255$ nm and $z = 295$ nm are at the middle of the first and second tungsten octagonal prisms, they are suitable to be selected as the typical planes to illustrate the dissipation mechanisms of electromagnetic waves within the tungsten octagonal prisms. The $|\boldsymbol{E}|$ distributions in these two planes are shown in Fig. 3c and d, respectively. It can be seen in Fig. 3c and d that regions with strong $|\boldsymbol{E}|$ are strongly concentrated at the vertexes of the first and the second tungsten octagonal prisms, which suggests that the local surface plasmon resonances (LSPRs) are excited. In addition, the $|\boldsymbol{E}|$ increases with rising wavelength, indicating that the intensity of LSPRs increases with rising wavelength.

Finally, the energy transport and absorption of the electromagnetic waves are also visually presented in Fig. 3. As can be seen from Fig. 3, most of the Poynting vectors (white arrows) point to four components, including the two tungsten octagonal prisms, and the two tungsten films. This is because there are multiple plasmonic modes in these parts, efficiently converting solar radiation to thermal energy due to ohmic loss.

As discussed above, it can be concluded that the coupling of SPPs, MPs and the LSPRs leads to the good absorption of the radiation within the solar spectrum.

Then, to better explore the absorption mechanisms of the near-perfect MA, the impedance matching of the MA and the free space was studied. The relation between effective impedance ($z_\lambda$) and $S$ parameters can be described by eqn (7).[50,51]

$$z_\lambda = \sqrt{\frac{(1+S_{11})^2 - S_{21}^2}{(1-S_{11})^2 - S_{21}^2}} \tag{7}$$

where the $S_{11}$ and $S_{21}$ are the scattering matrix coefficients of the reflection.

Furthermore, the relation between the $z_\lambda$ and the $\alpha_\lambda$ can be expressed by eqn (8).[44] According to eqn (8), perfect spectral absorptivity ($\alpha_\lambda$) can be achieved when the effective impedance $z_\lambda$ is matched to the impedance of the free space ($z_0$), as shown in eqn (9). In addition, near-zero absorptivity will be achieved when eqn (10) is met.

$$\alpha_\lambda = \frac{4\mathrm{Re}(z_\lambda)}{[1+\mathrm{Re}(z_\lambda)]^2 + [\mathrm{Im}(z_\lambda)]^2} \tag{8}$$

$$\mathrm{Re}(z_\lambda) = \mathrm{Re}(z_0) = 1,\ \mathrm{Im}(z_\lambda) = \mathrm{Im}(z_0) = 0 \tag{9}$$

$$\mathrm{Re}(z_\lambda) = 0,\ \mathrm{Im}(z_\lambda) = 1 \tag{10}$$

where $\mathrm{Im}(z_\lambda)$ and $\mathrm{Re}(z_\lambda)$ are the imaginary and real parts of $z_\lambda$ of the MA, respectively; $\mathrm{Im}(z_0)$ and $\mathrm{Re}(z_0)$ are the imaginary and real parts of $z_0$ of the free space, respectively.

The imaginary part $\mathrm{Im}(z_\lambda)$ and real part $\mathrm{Re}(z_\lambda)$ of the effective impedance $z_\lambda$ of the near-perfect MA are calculated and illustrated in Fig. 4. It is manifest from the Fig. 4 that $\mathrm{Im}(z_\lambda)$ and $\mathrm{Re}(z_\lambda)$ are nearly 0 and 1 within $\lambda = 0.373$–$1.656$ μm, which agrees with the near-perfect $\alpha_\lambda$ (>0.98) within this region in Fig. 4. Furthermore, the $\mathrm{Im}(z_\lambda)$ and $\mathrm{Re}(z_\lambda)$ appear dramatic changes within $\lambda = 2$–$3.5$ μm, which causes a rapid decrease in the $\alpha_\lambda$. Meanwhile, $\mathrm{Im}(z_\lambda)$ and $\mathrm{Re}(z_\lambda)$ are close to 1 and 0, respectively, when $\lambda > 3.5$ μm, which leads to almost 0 of the $\alpha_\lambda$. The above results indicate that the impedance of the near-

Open Access Article. Published on 07 June 2022. Downloaded on 7/28/2024 11:16:37 PM.
This article is licensed under a Creative Commons Attribution-NonCommercial 3.0 Unported Licence.

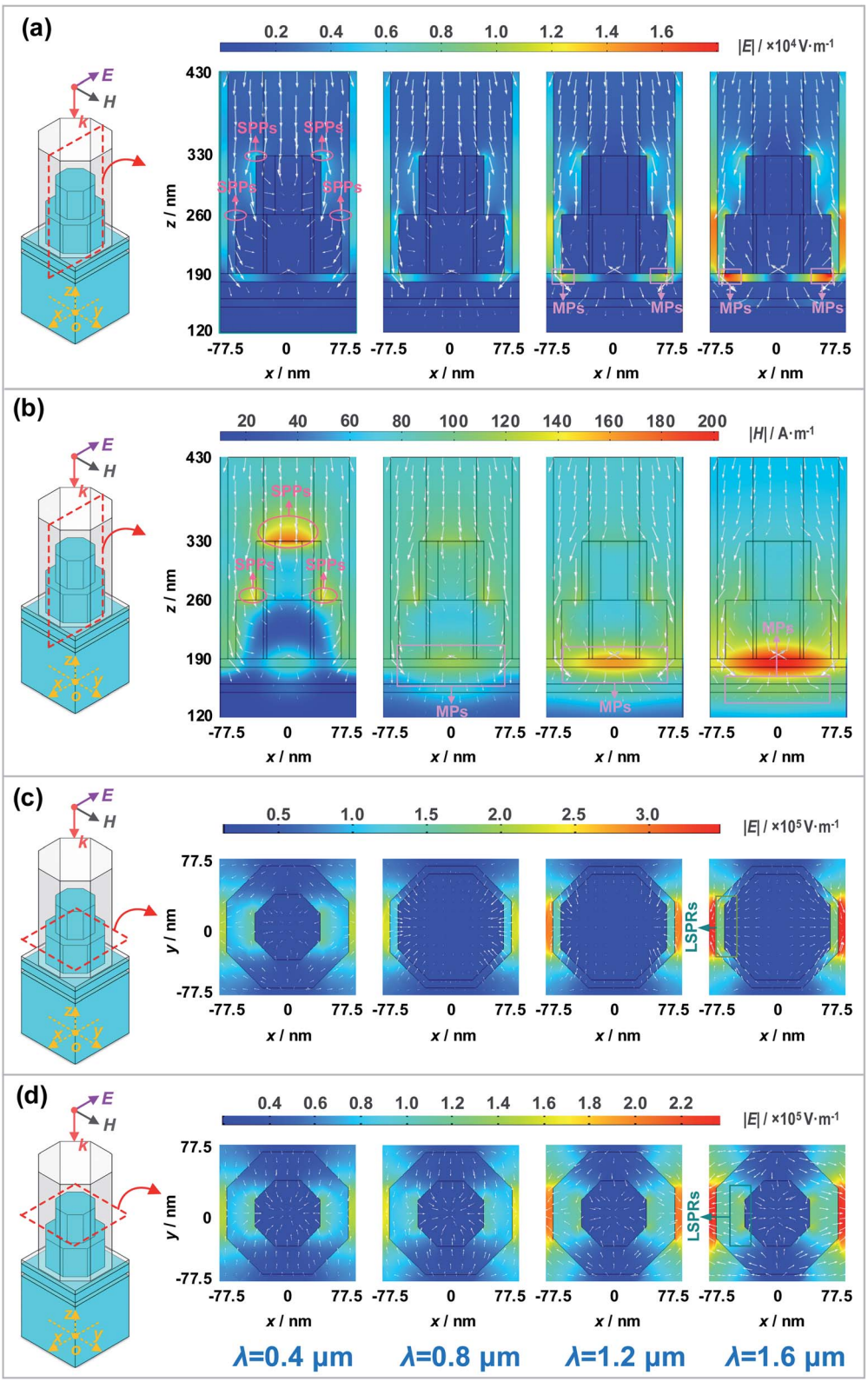


Fig. 3 Distributions of the $|E|$, $|H|$ and Poynting vectors (white arrows) at various wavelengths. (a) $|E|$ in the $xz$ plane at $y = 0$ nm; (b) $|H|$ in the $xz$ plane at $y = 0$ nm; (c) $|E|$ in the $xy$ plane at $z = 225$ nm; (d) $|E|$ in the $xy$ plane at $z = 295$ nm.

perfect MA highly matches that of the free space within $\lambda = 0.373$–$1.656$ μm, but they doesn't match with each other at all when $\lambda > 3.5$ μm.

Then, to investigate the energy absorption capacities of different components in the near-perfect MA, the spectral absorptivity of the five components was studied. It can be


© 2022 The Author(s). Published by the Royal Society of Chemistry

Open Access Article. Published on 07 June 2022. Downloaded on 7/28/2024 11:16:37 PM.
This article is licensed under a Creative Commons Attribution-NonCommercial 3.0 Unported Licence.

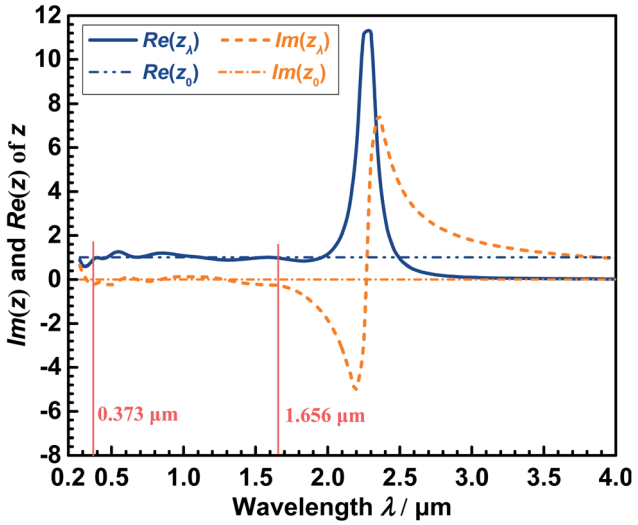


Fig. 4 The imaginary part Im($z_\lambda$) and real part Re($z_\lambda$) of the $z_\lambda$ of the near-perfect MA.

observed from Fig. 5a that the prisms play significant roles in enhancing the absorption performance, and the first and the second tungsten films also contribute some $\alpha_\lambda$. This is because the prisms introduce multiple resonance modes which enhance the transports of the electromagnetic waves in the tungsten, where the electromagnetic waves are dissipated quickly due to ohmic loss. Meanwhile, the $\alpha_\lambda$ curves of the first and the second $SiO_2$ films are close to zero within the whole solar spectrum. However, the two films are still necessary for improving the $\alpha_\lambda$, because they can be combined with adjacent tungsten components to build a metal–dielectric–metal structure for exciting MPs, and also can protect the MA from being oxidized.

In addition, to analyze the influences of the prisms in the near-perfect MA, the prisms are divided into three layers in Fig. 5b. It is manifest from the Fig. 5b that the $\alpha_\lambda$ of the layer 1, layer 2 and layer 3 are approximately 0.9–47.1%, 0.3–60.7%, and ~0 when $\lambda$ = 0.28–4.0 μm, respectively. As the wavelength increases, the $\alpha_\lambda$ of layer 2 decreases gradually, resulting in the decrease in the $\alpha_\lambda$ of the prisms. However, the $\alpha_\lambda$ values of the first and the second tungsten films are increased at the same time (see Fig. 5a), so the $\alpha_\lambda$ of the MA is near perfect within $\lambda$ = 0.373–1.656 μm. Meanwhile, the $\alpha_\lambda$ of layer 3 is nearly zero, which suggests that this layer barely absorbs the electromagnetic waves. Nevertheless, layer 3 is also essential for the MA, because it can protect the MA from oxidation.

### 4.3 Influences of structure parameters on the spectral absorptivity

According to the analysis in the previous section, the excellent spectral selectivity of the near-perfect MA is due to the coupling effects of multi-plasmon resonance modes and the impedance matching with the free space at octagonal prisms and underneath films. However, the influences of their structure parameters on the absorption performance of the MA are still unclear. Therefore, geometric influences on the spectral absorptivity were analyzed in this section. Meanwhile, it should be noted that the other parameters remained identical to the optimal parameter values when one parameter was analyzed.

**4.3.1 Influences of the structure parameters of tungsten octagonal prisms.** The parameters related to the octagonal prisms are the excircle diameters of the first ($d_2$) and the second ($d_3$) tungsten octagonal prisms, and the heights of the first ($h_6$) and the second ($h_7$) tungsten octagonal prisms. According to the above discussion, the octagonal prisms have important influences on the spectral absorptivity ($\alpha_\lambda$) of the MA. Hence, the influences of the four parameters were studied, and the results are presented in Fig. 6.

It is manifest from the Fig. 6a that the $\alpha_\lambda$ ascends obviously with increasing $d_2$ in the whole solar spectrum region. This is because the first tungsten octagonal prism can not only excite SPPs and LSPRs, but also can excite MPs together with the second $SiO_2$ film and the second tungsten film. Therefore, $d_2$ has a great influence on the $\alpha_\lambda$ of the MA. As shown in Fig. 6b, when $h_6$ = 0.06–0.10 μm, the $\alpha_\lambda$ varies irregularly and slightly within $\lambda$ = 0.28–1.8 μm, however it increases slightly with increasing $h_6$ when $\lambda$ > 1.8 μm. In addition, when the $h_6$ increases from 0.1 μm to 0.30 μm, the $\alpha_\lambda$ declines sharply within $\lambda$ = 1.0–2.2 μm but increases obviously within $\lambda$ = 2.2–4.0 μm.

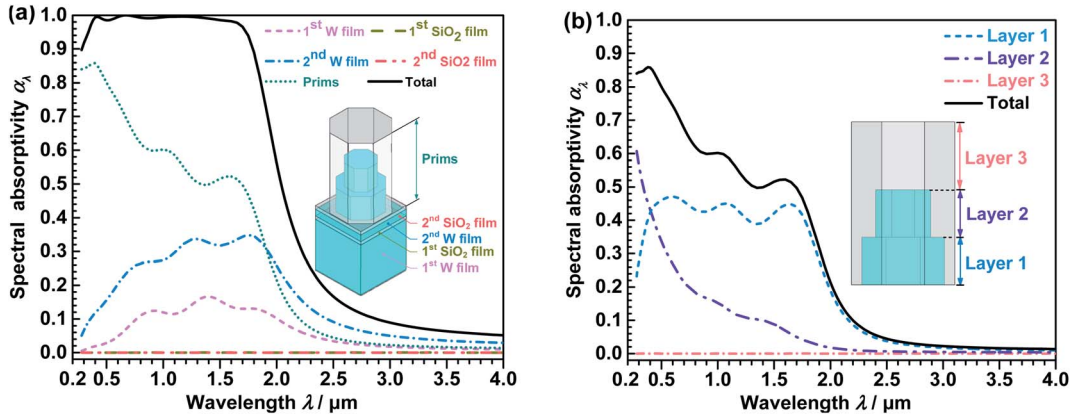


Fig. 5 Spectral absorptivity ($\alpha_\lambda$) of different parts of the near-perfect MA. (a) $\alpha_\lambda$ of different components; (b) $\alpha_\lambda$ of different layers of the prims.

Open Access Article. Published on 07 June 2022. Downloaded on 7/28/2024 11:16:37 PM.
This article is licensed under a Creative Commons Attribution-NonCommercial 3.0 Unported Licence.

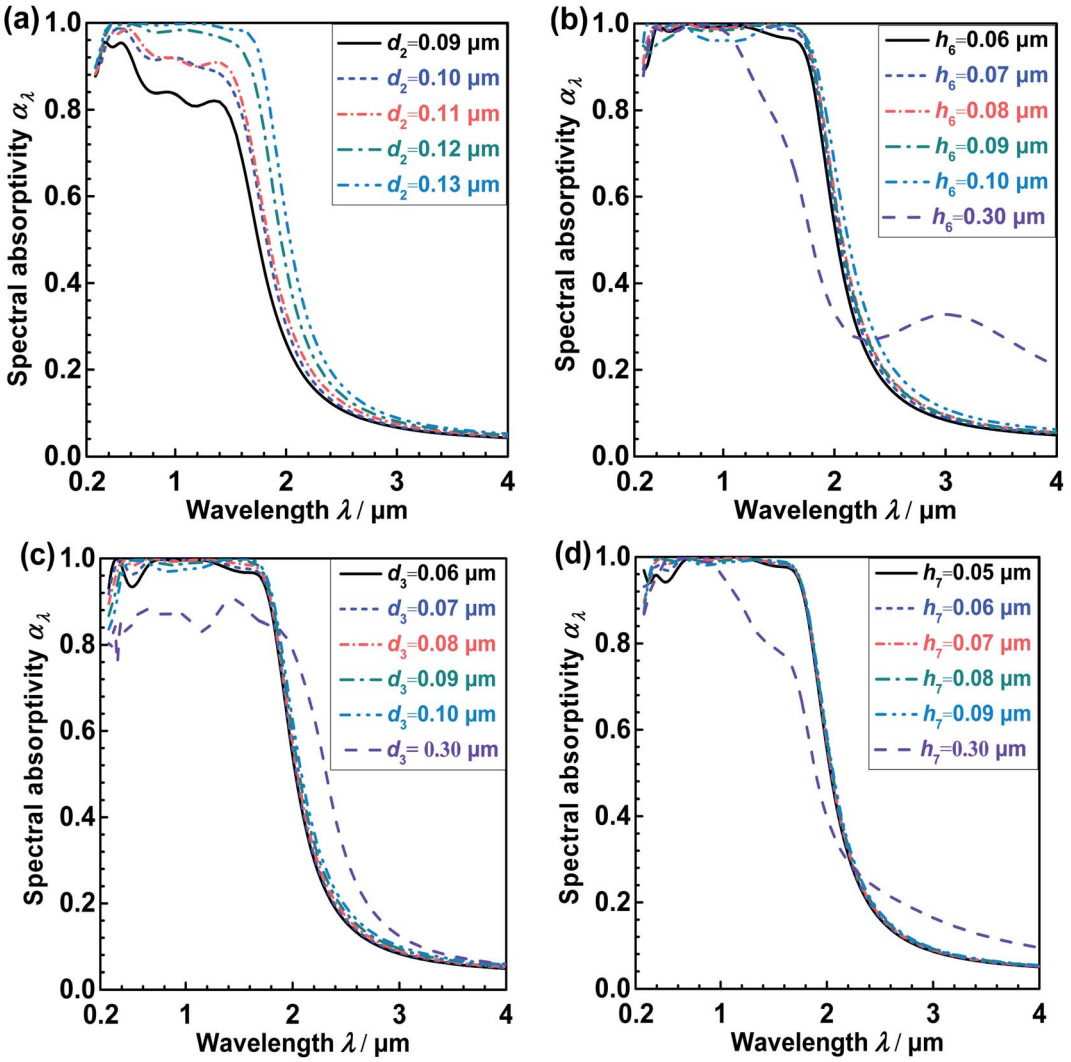


Fig. 6 Spectral absorptivity ($\alpha_\lambda$) of the MA at different structure parameters of tungsten octagonal prisms. (a) Influences of $d_2$; (b) influences of $h_6$; (c) influences of $d_3$; (d) influences of $h_7$.

As shown in Fig. 6c, when $d_3$ = 0.06–0.10 μm, the $\alpha_\lambda$ increases slightly when $\lambda$ is around 0.4 μm but decreases appreciably within $\lambda$ = 0.28–2.0 μm with increasing $d_3$. Moreover, $\alpha_\lambda$ increases significantly within $\lambda$ = 2.2–4.0 μm when $d_3$ increases from 0.10 μm to 0.30 μm. As is presented in Fig. 6d, the increase in $h_7$ has a little influence on the $\alpha_\lambda$ within $\lambda$ = 0.28–4 μm when $h_6$ = 0.05–0.09 μm. However, the $\alpha_\lambda$ declines dramatically within $\lambda$ = 0.8–2.2 μm and increases obviously within $\lambda$ = 2.2–4.0 μm when the $h_7$ increases to 0.30 μm.

To sum up, all the parameters related to the octagonal prisms will affect $\alpha_\lambda$ of the MA. It is known that the fabrication uncertainties of the absorber are smaller than 0.01 μm.[52] When the variations of these parameters are within the fabrication uncertainties, only the $d_2$ has obvious influences on the $\alpha_\lambda$, indicating that $d_2$ should be controlled carefully in the fabrication. However, $h_6$, $d_3$, and $h_7$ influence $\alpha_\lambda$ slightly, indicating that these geometries are able to sustain relatively large fabrication uncertainties.

**4.3.2 Influences of the structure parameters of underneath films.** The parameters that are relevant to the underneath films are the height of the first $SiO_2$ film ($h_2$), the height of the second tungsten film ($h_3$), the height of the second $SiO_2$ film ($h_4$). The influences of the three parameters on the spectral absorptivity ($\alpha_\lambda$) are shown in Fig. 7.

It can be found from Fig. 8a that the $\alpha_\lambda$ remains virtually unchanged within $\lambda$ = 0.28–1.8 μm when $h_2$ increases from 0.01 μm to 0.05 μm, but $\alpha_\lambda$ declines obviously when $h_2$ increases from 0.05 μm to 0.20 μm. In addition, the $\alpha_\lambda$ exhibits an upward trend with the increase in $h_2$ when $\lambda$ is larger than 1.8 μm within $h_2$ = 0.01–0.05 μm. Moreover, the increase in $\alpha_\lambda$ is significant when the $h_2$ increases to 0.20 μm within $\lambda$ > 1.8 μm. As shown in Fig. 8b, the $\alpha_\lambda$ varies slightly when $h_3$ = 0.01–0.20 μm within $\lambda$ = 0.28–4 μm, suggesting that this parameter has little influences on the absorption performance. It is manifest from the Fig. 8c that the $\alpha_\lambda$ declines gradually with increasing $h_4$ within 0.3–2 μm, but the $\alpha_\lambda$ hardly changes as $h_4$ changes when $\lambda$ = 2–4 μm.


© 2022 The Author(s). Published by the Royal Society of Chemistry

Open Access Article. Published on 07 June 2022. Downloaded on 7/28/2024 11:16:37 PM.
This article is licensed under a Creative Commons Attribution-NonCommercial 3.0 Unported Licence.

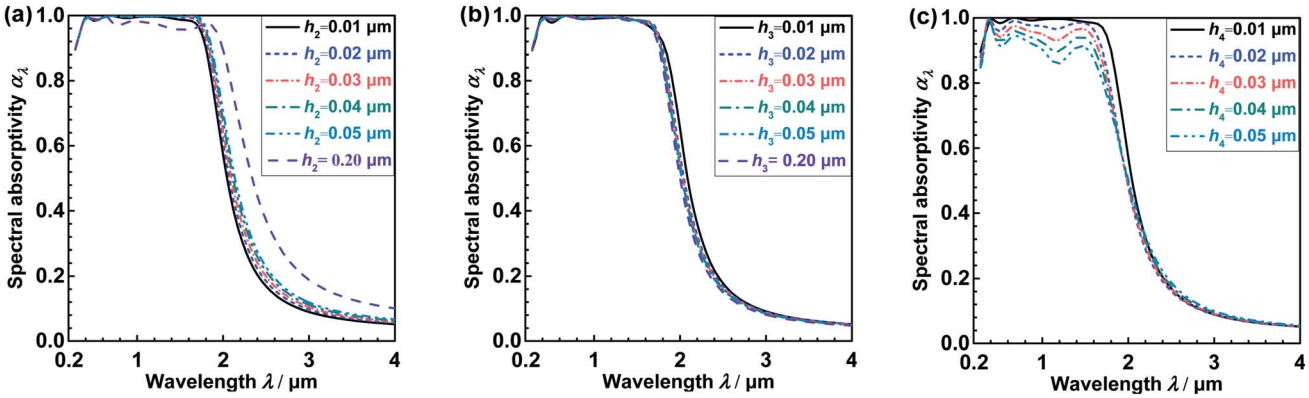


Fig. 7 Spectral absorptivity ($\alpha_\lambda$) of the MA at different structure parameters of underneath films (a) influences of $h_2$; (b) influences of $h_3$; (c) influences of $h_4$.

To sum up, the $h_4$ has obviously influences on the $\alpha_\lambda$ of the MA when $\lambda = 0.35$–2 μm, but the $h_2$ has slight influences on the $\alpha_\lambda$ within the fabrication uncertainty. And the $h_3$ influences little on the $\alpha_\lambda$ when $h_3 = 0.01$–0.20 μm.

### 4.4 Influences of incident angle and polarization angle

The incident and polarization angles of realistic solar radiation are variational in practical applications, and the MA should be insensitive to these angles for converting radiation into heat effectively. Therefore, the sensitivities of the near-perfect MA to the incident angle $\theta$ and polarization angle $\varphi$ (seen Fig. 1c) were studied within $\lambda = 0.28$–4.0 μm in this section.

The influences of the $\theta$ of TE and TM polarized waves on the $\alpha_\lambda$ of the near-perfect MA were evaluated, as shown in Fig. 8. It can be observed from Fig. 8a that the $\alpha_\lambda$ of the near-perfect MA changes 5% or less when the $\theta$ of the TE polarized wave increases from 0° to 50° within $\lambda = 0.33$–1.92 μm. Moreover, as seen in Fig. 8b, the $\alpha_\lambda$ changes 5% or less when the $\theta$ of the TM polarized wave increases from 0° to 50° within 0.28–1.27 μm and 2.44–3.00 μm.

Meanwhile, the solar absorptivity ($\alpha_{sol}$) of the near-perfect MA under TE and TM polarized waves with various incident angles are shown in Fig. 9. As can be seen in Fig. 9, when the $\theta$ is within 0–50°, the solar absorptivity ($\alpha_{sol}$) of 0.9591–0.9572 and 0.9591–0.9471 were achieved by the TE and TM polarized waves, respectively. These results suggest that the near-perfect MA presents excellent insensitivity when the incident angle is within 0–50°.

In addition, it can be found from Fig. 10 that the $\alpha_\lambda$ of the near-perfect MA is almost unchanged when the $\varphi$ of the normally incident wave increases from 0° to 90°. The results indicate that the near-perfect MA is completely insensitive to the $\varphi$ in Fig. 1c when $\lambda = 0.28$–4.0 μm. Moreover, because the near-perfect MA is rotationally symmetric, its $\alpha_\lambda$ under normally incident TE polarized wave (*i.e.* the electric field is in the $y$ direction) and TM polarized wave are the same. Additionally, the symmetric structure of the near-perfect MA is also the main reason to obtain excellent polarization insensitivity.[17]

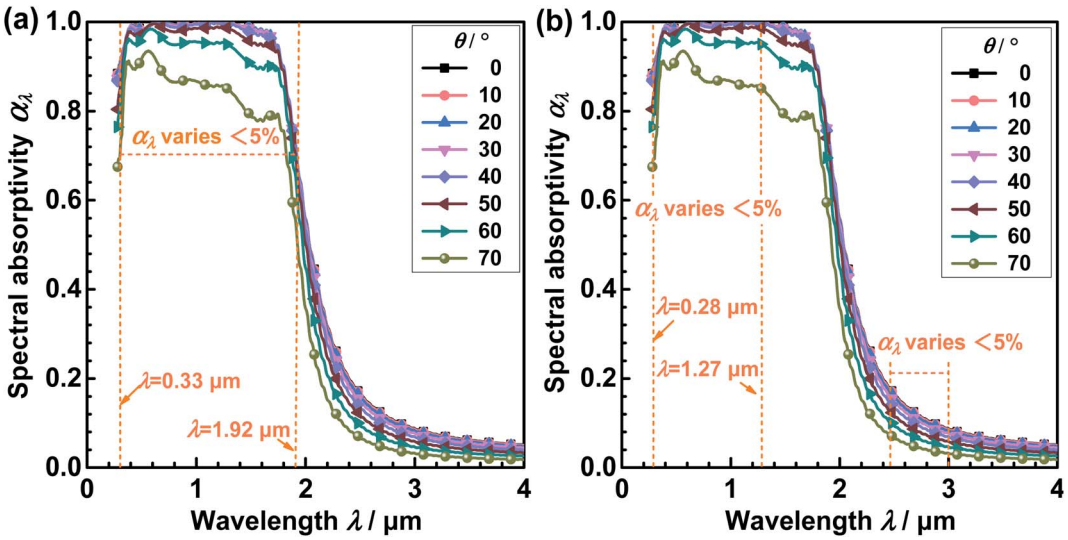


Fig. 8 Spectral absorptivity ($\alpha_\lambda$) under various incident angles ($\theta$). (a) $\alpha_\lambda$ of TE wave. (b) $\alpha_\lambda$ of TM wave.

Open Access Article. Published on 07 June 2022. Downloaded on 7/28/2024 11:16:37 PM.
This article is licensed under a Creative Commons Attribution-NonCommercial 3.0 Unported Licence.

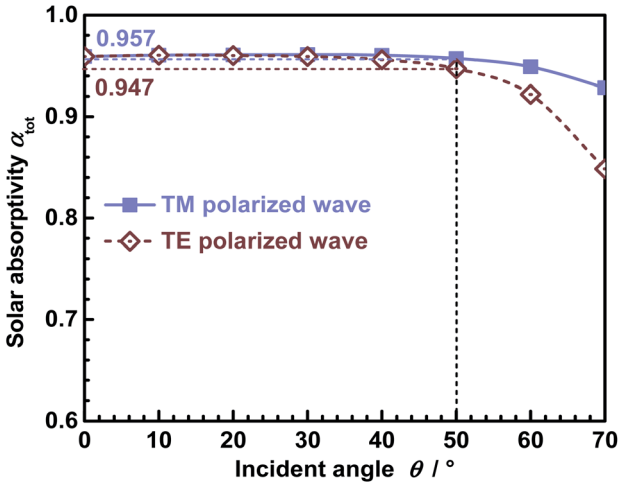


Fig. 9 Solar absorptivity ($\alpha_{sol}$) of the MA under TE and TM polarized waves with various incident angles.

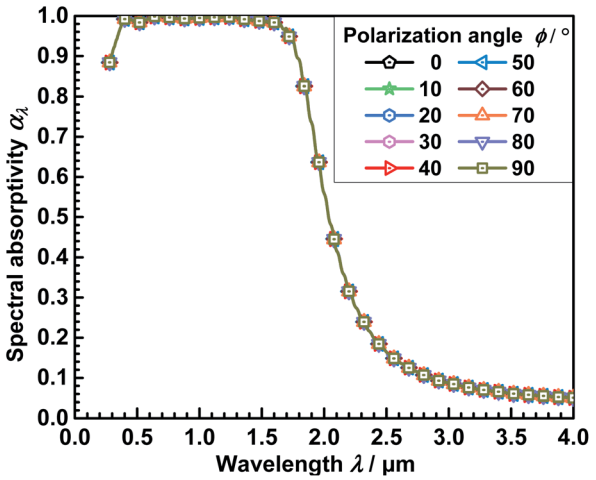


Fig. 10 Spectral absorptivity ($\alpha_\lambda$) under normally incident wave with various polarization angles ($\varphi$).

## 5. Conclusions

In this article, a near-perfect spectrally-selective metasurface solar absorber consisting of an octagonal prism array is designed and investigated for solar energy harvesting at high temperatures, and the following conclusions are obtained.

(1) A near-perfect spectrally-selective absorber with $p$ = 155 nm, $h_1$ = 150 nm, $h_2$ = 10 nm, $h_3$ = 20 nm, $h_4$ = 10 nm, $d_1$ = 150 nm, $h_5$ = 240 nm, $d_2$ = 130 nm, $h_6$ = 70 nm, $d_3$ = 80 nm, and $h_7$ = 70 nm was obtained after optimizing the metasurface structure. The high solar absorptivity of 0.9591 and a low emissivity of 0.1594–0.3694 were achieved by the near-perfect absorber, leading to high photothermal efficiency of 94.72–83.10% under 1000 suns and 1073–1573 K.

(2) The underlying absorption mechanisms leading to the spectral selective absorption of this near-perfect absorber were revealed. It is found that coupling effects of multi-plasmon resonance modes combined with the impedance matching with the free space lead to the high solar absorptivity. Moreover, the impedance mismatching is the mechanism to minimize the emissivity in the mid-IR region.

(3) Influences of the structure parameters of the absorber are studied. The results suggest that the excircle diameter of the first tungsten octagonal prism and the height of the $SiO_2$ under the octagonal prism have stronger influences on the spectral absorptivity than other parameters within the fabrication uncertainty.

(4) Sensitivities of the near-perfect absorber to the incident angle ($\theta$) and polarization angle ($\varphi$) are investigated. The solar absorptivity of 0.9591–0.9572 and 0.9591–0.9471 are achieved under TE and TM polarized waves within $\theta$ = 0–50°, respectively. And the $\alpha_\lambda$ of the near-perfect MA is almost unchanged within $\varphi$ = 0–90°. These results demonstrate that the near-perfect absorber is insensitive to the incident angle within $\theta$ = 0–50° and polarization angle within $\varphi$ = 0–90°.

## Abbreviations

| | |
|---|---|
| $C$ | Solar concentration ratio |
| $d_1$ | Excircle diameter of the $SiO_2$ octagonal prism (nm) |
| $d_2$ | Excircle diameter of the first tungsten octagonal prism (nm) |
| $d_3$ | Excircle diameter of the second tungsten octagonal prism (nm) |
| $\boldsymbol{E}$ | Electric field (V $m^{-1}$) |
| $h_1$ | Height of the first tungsten film (nm) |
| $h_2$ | Height of the first $SiO_2$ film (nm) |
| $h_3$ | Height of the second tungsten film (nm) |
| $h_4$ | Height of the second $SiO_2$ film (nm) |
| $h_5$ | Height of the $SiO_2$ octagonal prism (nm) |
| $h_6$ | Height of the first tungsten octagonal prism (nm) |
| $h_7$ | Height of the second tungsten octagonal prism (nm) |
| $\boldsymbol{H}$ | Magnetic field (A $m^{-1}$) |
| $I_s$ | Solar flux intensity at AM1.5, 1000 W $m^{-2}$ |
| $I_{AM1.5}(\lambda)$ | Spectral solar irradiance at AM1.5 (W $m^{-2}$ $m^{-1}$) |
| $I_B(\lambda, T_{abs})$ | Spectral irradiance of blackbody (W $m^{-2}$ $m^{-1}$) |
| LSPRs | Local Surface Plasmon Resonances |
| MPs | Magnetic Polaritons |
| $\boldsymbol{r}_{dst}$ | Destination origin |
| $\boldsymbol{r}_{src}$ | Source origin |
| SPPs | Surface Plasmon Polaritons |
| $S_{11}$, $S_{21}$ | Scattering matrix coefficients |
| $T_{abs}$ | Temperature of metasurface (K) |
| $T_{amb}$ | Temperature of ambient (K) |
| $z_\lambda$ | Effective impedance of metasurface |
| $xyz$ | Cartesian coordinates (nm) |
| $\alpha_{sol}$ | Solar absorptivity |
| $\alpha_\lambda$ | Spectral absorptivity |
| $\varepsilon_{tot}$ | Total emissivity |
| $\eta$ | Photothermal efficiency (%) |
| $\theta$ | Incident angle (°) |
| $\lambda$ | Wavelength (μm) |
| $\rho_\lambda$ | Spectral reflectance |


© 2022 The Author(s). Published by the Royal Society of Chemistry

Open Access Article. Published on 07 June 2022. Downloaded on 7/28/2024 11:16:37 PM. This article is licensed under a Creative Commons Attribution-NonCommercial 3.0 Unported Licence.

| | |
|---|---|
| $\varphi$ | Polarization angle (°) |

## Author contributions

Mingpan Xu: conceptualization, methodology, validation, investigation, visualization, writing – original draft; Lin Guo: methodology, validation, investigation, visualization, writing – original draft; Pengfei Zhang: methodology, validation, investigation, visualization, writing – original draft; Yu Qiu: conceptualization, methodology, investigation, writing – original draft, writing – review & editing, supervision; Qing Li: methodology, formal analysis, writing – review & editing, supervision; Jikang Wang: formal analysis, visualization.

## Conflicts of interest

The authors declare that they have no known competing financial interests or personal relationships that could have appeared to influence the work reported in this paper.

## Acknowledgements

This work was supported by the National Natural Science Foundation of China (No.52006247, No.52176093). The authors will also like to thank the Natural Science Foundation of Hunan Province (2021JJ40753), the Natural Science Foundation of Shandong Province (No. ZR2021QE078), and the Collaborative Innovation Project of Colleges in Jinan (No. 2021GXRC059).

## References

1 X. Zheng, D. Qu, Y. Bao, G. Qin, Y. Liu and Q. Luo, *J. Chem. Eng. Data*, 2022, **67**(1), 45–53.
2 Y. Dong, H. Han, Y. Qiu, F. Wang, Y. Zhang, Z. Cheng, X. Shi and Y. Yan, *Renewable Energy*, 2022, **192**, 606–616.
3 Q. Li, Y. Zhang, Z. Wen and Y. Qiu, *Energy Convers. Manage.*, 2020, **214**, 112911.
4 K. Wang, P. S. Jia, Y. Zhang, Z. D. Zhang, T. Wang and C. H. Min, *Sol. Energy*, 2021, **223**, 72–86.
5 Y. Zhang, Y. Qiu, Q. Li and A. Henry, *Appl. Energy*, 2021, **307**, 118228.
6 Y. Qiu, M. Xu, Q. Li, Y. Xu and J. Wang, *Energy Convers. Manage.*, 2021, **227**, 113589.
7 Z. Wu, J. Wang, Y. Liu, S. Hou, X. Liu, Q. Zhang and F. Cao, *Mater. Today Phys.*, 2021, **18**, 100388.
8 C. Y. He, X. H. Gao, D. M. Yu, X. L. Qiu, H. X. Guo and G. Liu, *J. Mater. Chem. A*, 2021, **9**, 6413–6422.
9 X. L. Qiu, C. Y. He, P. Zhao, B. H. Liu, H. X. Guo, G. Liu and X. H. Gao, *Mater. Today Phys.*, 2022, **24**, 100690.
10 A. Dan, A. Soum Glaude, A. Carling Plaza, C. K. Ho, K. Chattopadhyay, H. C. Barshilia and B. Basu, *ACS Appl. Energy Mater.*, 2019, **2**, 5557–5567.
11 Z. Nuru, M. Msimanga, C. Arendse and M. Maaza, *Appl. Surf. Sci.*, 2014, **298**, 176–181.
12 Y. Tian, X. Liu, A. Ghanekar and Y. Zheng, *Appl. Energy*, 2021, **281**, 116055.
13 H. Wang, H. Alshehri, H. Su and L. Wang, *Sol. Energy Mater. Sol. Cells*, 2018, **174**, 445–452.
14 A. AL-Rjoub, L. Rebouta, P. Costa and L. Vieira, *Sol. Energy Mater. Sol. Cells*, 2018, **186**, 300–308.
15 X. Wang, X. Zhang, Q. Li, J. Min and X. Cheng, *Sol. Energy Mater. Sol. Cells*, 2018, **188**, 81–92.
16 F. Zhao, J. Lin, Z. Lei, Z. Yi, F. Qin, J. Zhang, L. Liu, X. Wu, W. Yang and P. Wu, *Phys. Chem. Chem. Phys.*, 2022, **24**, 4871–4880.
17 F. Zhou, F. Qin, Z. Yi, W. Yao, Z. Liu, X. Wu and P. Wu, *Phys. Chem. Chem. Phys.*, 2021, **23**, 17041–17048.
18 Z. Liu, G. Liu, Z. Huang, X. Liu and G. Fu, *Sol. Energy Mater. Sol. Cells*, 2018, **179**, 346–352.
19 M. Chen and Y. He, *Sol. Energy Mater. Sol. Cells*, 2018, **188**, 156–163.
20 D. Wu, C. Liu, Y. Liu, Z. Xu, Z. Yu, L. Yu, L. Chen, R. Ma, J. Zhang and H. Ye, *RSC Adv.*, 2018, **8**, 21054–21064.
21 X. Jiang, T. Wang, Q. Zhong, R. Yan and X. Huang, *Nanotechnology*, 2020, **31**, 315202.
22 M. M. Hassan, F. Islam, M. Z. Baten and S. Subrina, *RSC Adv.*, 2021, **11**, 37595–37603.
23 Y. Qiu, Y. Xu, Q. Li, J. Wang, Q. Wang and B. Liu, *Appl. Energy*, 2021, **299**, 117290.
24 Z. Liu, G. Duan, H. Duan and Z. Wang, *Sol. Energy Mater. Sol. Cells*, 2022, **240**, 111688.
25 Z. Wang and P. Cheng, *Int. J. Heat Mass Transfer*, 2019, **140**, 453–482.
26 Y. Qiu, P. Zhang, Q. Li, Y. Zhang and W. Li, *Sol. Energy*, 2021, **230**, 1165–1174.
27 C. C. Chang, W. J. Kort Kamp, J. Nogan, T. S. Luk, A. K. Azad, A. J. Taylor, D. A. Dalvit, M. Sykora and H. T. Chen, *Nano Lett.*, 2018, **18**, 7665–7673.
28 J. C. Maxwell, *A treatise on electricity and magnetism*, Clarendon press, New York, 1873.
29 E. D. Palik, *Handbook of optical constants of solids*, Academic press, San Diego, California, 1998.
30 A. D. Rakić, A. B. Djurišić, J. M. Elazar and M. L. Majewski, *Appl. Opt.*, 1998, **37**, 5271–5283.
31 *COMSOL Multiphysics 5.6*, COMSOL Inc, 2020, **https://www.comsol.com/**.
32 Z. Zheng, Y. Luo, H. Yang, Z. Yi, J. Zhang, Q. Song, W. Yang, C. Liu, X. Wu and P. Wu, *Phys. Chem. Chem. Phys.*, 2022, **24**, 8846–8853.
33 Z. Zheng, Y. Zheng, Y. Luo, Z. Yi, J. Zhang, Z. Liu, W. Yang, Y. Yu, X. Wu and P. Wu, *Phys. Chem. Chem. Phys.*, 2022, **24**, 2527–2533.
34 Y. Tian, X. Liu, F. Chen and Y. Zheng, *OSA Continuum*, 2019, **2**, 3223–3239.
35 F. Cao, K. McEnaney, G. Chen and Z. Ren, *Energy Environ. Sci.*, 2014, **7**, 1615–1627.
36 Air Mass 1.5 Spectra, American Society for Testing and Materials (ASTM), available from **https://www.nrel.gov/grid/solar-resource/spectra.html**.
37 A. Narayanaswamy, S. Shen, L. Hu, X. Chen and G. Chen, *Appl. Phys. A*, 2009, **96**, 357–362.
38 Q. Wang, H. Yang, M. Hu, J. Cao, G. Pei and H. Yang, *J. Cleaner Prod.*, 2021, **278**, 123407.

© 2022 The Author(s). Published by the Royal Society of Chemistry

Open Access Article. Published on 07 June 2022. Downloaded on 7/28/2024 11:16:37 PM.
This article is licensed under a Creative Commons Attribution-NonCommercial 3.0 Unported Licence.

39 Q. Wang, M. Hu, H. Yang, J. Cao, J. Li, Y. Su and G. Pei, *Renewable Energy*, 2019, **138**, 793–804.
40 X. Wang, E. Lee, C. Xu and J. Liu, *Mater. Today Energy*, 2021, **19**, 100609.
41 K. Niranjan, A. Soum Glaude, A. Carling Plaza, S. Bysakh, S. John and H. C. Barshilia, *Sol. Energy Mater. Sol. Cells*, 2021, **221**, 110905.
42 C. He, X. Gao, D. Yu, H. Guo, S. Zhao and G. Liu, *ACS Appl. Mater. Interfaces*, 2021, **13**, 16987–16996.
43 Q. Ye, M. Chen and W. Cai, *Sol. Energy*, 2019, **184**, 489–496.
44 J. Qian, J. Zhou, Z. Zhu, Z. Ge, S. Wu, X. Liu and J. Yi, *Nanomaterials*, 2021, **11**, 2709.
45 Y. Li, C. Lin, Z. Wu, Z. Chen, C. Chi, F. Cao, D. Mei, H. Yan, C. Y. Tso and C. Y. Chao, *Adv. Mater.*, 2021, **33**, 2005074.
46 S. s. Zhao, X. L. Qiu, C. Y. He, D. M. Yu, G. Liu and X. H. Gao, *ACS Appl. Nano Mater.*, 2021, **4**, 4504–4512.
47 A. Raza, A. S. Alketbi, R. Devarapalli, H. Li and T. Zhang, *Adv. Opt. Mater.*, 2020, **8**, 2000679.
48 X. L. Qiu, X. H. Gao, C. Y. He and G. Liu, *Opt. Mater.*, 2020, **100**, 109666.
49 C. Y. He, X. H. Gao, D. M. Yu, S. S. Zhao, H. X. Guo and G. Liu, *J. Mater. Chem. A*, 2021, **9**, 21270–21280.
50 X. Wu, Y. Zheng, Y. Luo, J. Zhang, Z. Yi, X. Wu, S. Cheng, W. Yang, Y. Yu and P. Wu, *Phys. Chem. Chem. Phys.*, 2021, **23**, 26864–26873.
51 H. Chen, Z. Chen, H. Yang, L. Wen, Z. Yi, Z. Zhou, B. Dai, J. Zhang, X. Wu and P. Wu, *RSC Adv.*, 2022, **12**, 7821–7829.
52 Y. Qiu, M. Xu, Q. Li, R. Huang and J. Wang, *ES Energy Environ.*, 2021, **13**, 77–90.
53 W. Wang, M. Li, R. Jiang, Y. Hu and Y. He, *Renewable Energy*, 2022, **185**, 159–171.
54 Q. Li, E. E, J. Wang and Y. Zhang, *Energy Convers. Manage.*, 2022, **260**, 115618.
55 Y. L. He, Y. Qiu, K. Wang, F. Yuan, W. Q. Wang, M. J. Li and J. Q. Guo, *Energy*, 2020, **198**, 117373.
56 Y. Qiu, Y. Zhang, Q. Li, Y. Xu and Z. X. Wen, *Appl. Energy*, 2020, **279**, 115810.
57 K. Wang, Z. D. Zhang, X. Y. Zhang and C. H. Min, *Int. J. Heat Mass Transfer*, 2021, **175**, 121130.


© 2022 The Author(s). Published by the Royal Society of Chemistry